LETTER

doi:10.1038/nature11492

En échelon and orthogonal fault ruptures of the 11 April 2012 great intraplate earthquakes

Han Yue[1], Thorne Lay[1] & Keith D. Koper[2]

The Indo-Australian plate is undergoing distributed internal deformation caused by the lateral transition along its northern boundary—from an environment of continental collision to an island arc subduction zone[1,2]. On 11 April 2012, one of the largest strike-slip earthquakes ever recorded (seismic moment magnitude M_w 8.7) occurred about 100–200 kilometres southwest of the Sumatra subduction zone. Occurrence of great intraplate strike-slip faulting located seaward of a subduction zone is unusual. It results from northwest–southeast compression within the plate caused by the India–Eurasia continental collision to the northwest, together with northeast–southwest extension associated with slab pull stresses as the plate underthrusts Sumatra to the northeast. Here we use seismic wave analyses to reveal that the 11 April 2012 event had an extraordinarily complex four-fault rupture lasting about 160 seconds, and was followed approximately two hours later by a great (M_w 8.2) aftershock. The mainshock rupture initially expanded bilaterally with large slip (20–30 metres) on a right-lateral strike-slip fault trending west-northwest to east-southeast (WNW–ESE), and then bilateral rupture was triggered on an orthogonal left-lateral strike-slip fault trending north-northeast to south-southwest (NNE–SSW) that crosses the first fault. This was followed by westward rupture on a second WNW–ESE strike-slip fault offset about 150 kilometres towards the southwest from the first fault. Finally, rupture was triggered on another *en échelon* WNW–ESE fault about 330 kilometres west of the epicentre crossing the Ninetyeast ridge. The great aftershock, with an epicentre located 185 kilometres to the SSW of the mainshock epicentre, ruptured bilaterally on a NNE–SSW fault. The complex faulting limits our resolution of the slip distribution. These great ruptures on a lattice of strike-slip faults that extend through the crust and a further 30–40 kilometres into the upper mantle represent large lithospheric deformation that may eventually lead to a localized boundary between the Indian and Australian plates.

It has long been recognized from relative plate motions that the Indo-Australian plate is not behaving as a single rigid unit[1]. Earthquake focal mechanisms, plate spreading rates inferred from magnetic lineations, fracture zone orientations, seismic stratigraphy, folds and sedimentary unconformities, and geodetic observations indicate diffuse internal deformation of the plate over a broad equatorial region (Fig. 1). This region extends from the central Indian ridge near the Chagos bank, eastward past the Ninetyeast ridge to the Sumatra trench[2–5], southward along the Ninetyeast ridge[6], and southeastward throughout the Wharton basin[5,7]. The southwestern part of the plate appears to have already fragmented to produce the Capricorn subplate[5,8], which has a diffuse border with the Australian plate along the southern Ninetyeast ridge. The NNE–SSW trends of the Ninetyeast ridge and fracture zones in the Wharton basin, together with aligned left-lateral strike-slip faulting mechanisms in both areas, may lead one to anticipate a similar orientation for any great rupture in the intraplate deformation zone. For example, the large 18 June 2000 (13.87° S, 97.3° E; M_w 7.9) earthquake in the Wharton basin appears to have involved predominantly left-lateral strike-slip faulting along the expected NNE–SSW orientation, although a second fault orientation was also activated during the 34-s-long rupture[9,10]. However, the east–west trend of the equatorial deformation zone raises the possibility of right-lateral faulting further north.

On 11 April 2012, a great intraplate earthquake (M_w 8.7) initiated at 2.31° N, 93.06° E at 08:38:37 UTC, followed by a great aftershock (M_w 8.2) at 0.77° N, 92.45° E at 10:43:09 UTC (Fig. 1)[11]. The overall faulting geometries of both events inferred from point-source moment

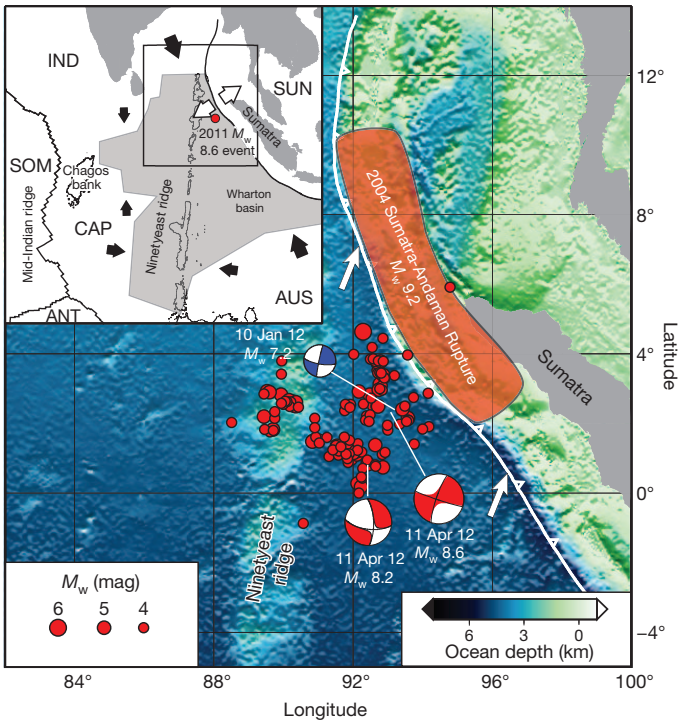

Figure 1 | The 11 April 2012 rupture sequence. Top inset, the regional plate tectonic setting, with the Indo-Australian plate being segmented into three subplates—India (IND), Australian (AUS) and Capricorn (CAP); also shown are the adjacent Somalian (SOM), Antarctic (ANT) and Sunda (SUN) plates. The light grey zone is a region of intraplate deformation between the subplates. Black arrows indicate directions of intraplate compression and white arrows show extension from subduction[5]. Major bathymetric features like the Chagos bank, Ninetyeast ridge and Wharton basin are indicated. Main panel, the USGS W-phase moment tensor solutions for the great events of 11 April 2012 (beachballs), USGS one-week aftershock locations (red circles with magnitude scale at lower left), and location and focal mechanism for the 10 January 2012 (M_w 7.2) event used as empirical Green functions in the surface wave analysis. The barbed line indicates the Sumatra trench, and the rupture zone of the M_w 9.2 Sumatra-Andaman underthrusting event[15] is shown. Bathymetry is shown, with the colour scale at the lower right. White arrows indicate the direction of motion of the Indo-Australian composite plate relative to the Sunda plate.

[1]Department of Earth and Planetary Sciences, University of California Santa Cruz, Santa Cruz, California 95064, USA. [2]Department of Geology and Geophysics, University of Utah, Salt Lake City, Utah 84112, USA.

tensor representations are similar (Fig. 1), with steeply dipping strike-slip orientations having either left-lateral slip on NNE–SSW faults or right-lateral slip on WNW–ESE faults, either of which would be consistent with the pervasive northwest–southeast compressional stress orientation throughout the region[7]. The first event is possibly the largest strike-slip earthquake ever seismically recorded (the 15 August 1950 Assam (M_w 8.6) interplate earthquake in the eastern Himalayas is of comparable size[12], but uncertain in faulting mechanism[13–15]), and it is probably the largest intraplate earthquake ever seismically recorded. This event triggered increases in seismicity globally[16]. The 2012 events are located 100–200 km seaward of the Sumatra subduction zone in which the Indo-Australian plate is underthrusting the Sunda plate, offshore of the epicentral region of the 26 December 2004 Sumatra-Andaman (M_w 9.2) interplate earthquake rupture (Fig. 1). The 2004 event involved 15–30 m of trench-perpendicular coseismic displacement on the plate boundary[17], and increased northeast horizontal extensional stress in the 2012 source region[18]. The ocean lithosphere varies in age from about 45 to 65 million years from east to west across the source region, although thermal rejuvenation along the Ninetyeast ridge may reduce the effective age there by up to 20 million years (ref. 19).

The relative epicentral locations of the two great events on 11 April 2012 immediately suggest rupture on a NNE–SSW-striking fault, and numerous rapid analyses of the seismic waves performed to characterize the space-time faulting history made this assumption; however, as more aftershock locations were determined, clear trends along parallel WNW–ESE lineations offset in latitude by ~150 km soon became apparent (Fig. 1). A robust seismic method for identifying fault planes and rupture spatial extent is by stacking short-period P-wave signals from networks of seismic stations at teleseismic distances corrected for propagation from a grid of possible source locations[20–23]. Within a few hours of the events, such semi-automated back-projections of short-period P waves from the mainshock recorded by networks of stations in Europe, China, Japan and Australia showed that pulses of coherent short-period seismic energy release appeared to illuminate both WNW aftershock trends, as well as additional loci of seismic radiation that were clearly not on a single NNE–SSW-oriented fault[24].

A summary of our own back-projections of short-period teleseismic P waves recorded by stations around Europe is presented in Fig. 2 (a time-varying animation is provided in Supplementary Movie 1). Coherent sources of short-period seismic energy radiation are imaged for more than 160 s and display a close correspondence with the regional distribution of epicentres of early (first-week) aftershocks, which are clearly on multiple faults. The initial rupture on the north-eastern WNW–ESE fault appears to expand bilaterally, with stronger radiation in the western part of the fault. After about 50 s the WNW rupture propagation ends, with a total fault length of about 150 km and a low overall rupture velocity of 1.5–2.0 km s^{-1}. Around 40 s into the rupture process, seismic radiation begins to be emitted from a perpendicular, presumably left-lateral conjugate plane that first ruptures 50–100 km in the SSW direction (from 30 to 60 s), then 50–100 km in the NNE direction (from 55 to 90 s). After about 70 s, seismic radiation continues on a second WNW–ESE fault that is roughly parallel to the first and separated by ~150 km to the southwest. This rupture propagates to the WNW, perhaps discontinuously, until about 145 s, at which time seismic radiation is apparent on a fourth distinct fault further to the west and persists until ~160 s. Also shown in Fig. 2 are back-projection results for the M_w 8.2 aftershock that commences just over 2 h later. The region of short-period energy release is much more compact than that of the mainshock, and the duration is roughly half as long (~80–85 s). The short-period energy release indicates bilateral rupture on a NNE–SSW plane with dominant propagation initially from the epicentre towards the NNE, consistent with the locations of early aftershocks, and weaker late energy release to the SSW.

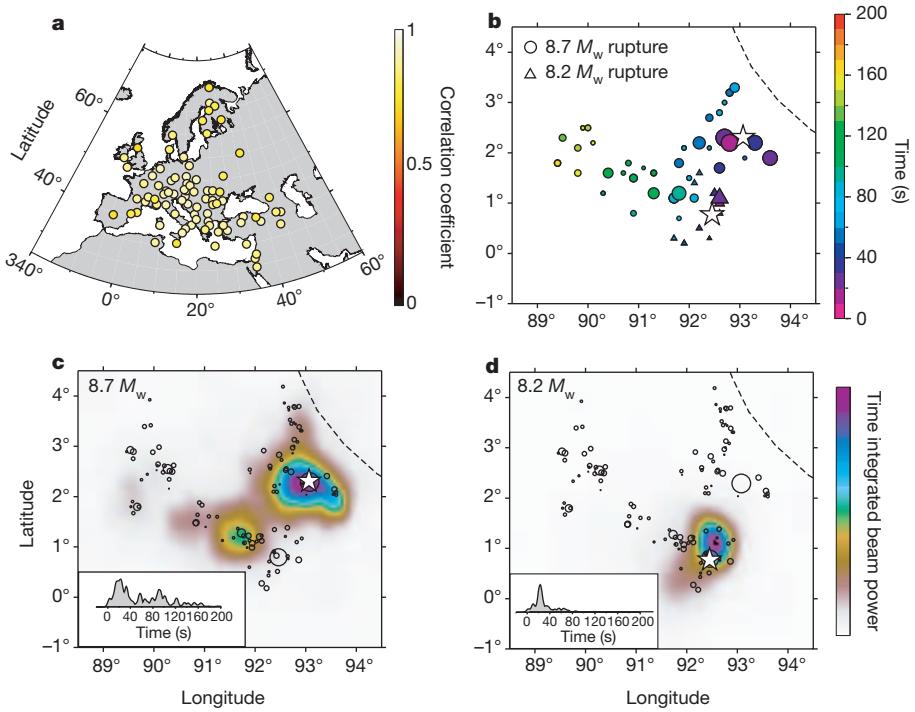

Figure 2 | Short-period seismic energy release pattern. **a**, Locations of seismograph stations in Europe that were used for the 0.5–2.0 Hz back-projection of the M_w 8.7 and M_w 8.2 Sumatra earthquakes. Signals were selected for high P-wave similarity (P-wave signal correlation coefficients relative to the array average are indicated) and a broad geographical distribution. **b**, Local beam power maxima during the back-projections, with colour indicating time after the nominal origin time. Symbol size is proportional to beam power. The dashed line is the location of the Sumatra trench. White stars are the epicentral locations of the M_w 8.7 and 8.2 earthquakes. **c**, Normalized time integrated relative beam power in units of $cm^2 s^{-2}$ (colour scale at right ranges linearly from white for zero to purple for unity) for the M_w 8.7 back-projection. The circles are early NEIC aftershocks with symbol size proportional to magnitude, and the dashed line is the Sumatra trench. The inset shows peak beam power as a function of time. **d**, Same as **c** but for the M_w 8.2 aftershock. The time-dependent behaviour is best evaluated by viewing Supplementary Movies 1 and 2.

Similar patterns of short-period radiation are observed for arrays of stations in Japan (see Supplementary Fig. 1 and Supplementary Movies 1 and 2), and by other investigators who have posted preliminary solutions online[24–27]. Using a lower-frequency passband of 0.1–0.5 Hz for the European P-wave observations smears the energy more broadly in space and accentuates the late energy in the mainshock rupture that occurs near longitudes of 89.5°–90.5° E, but otherwise gives results very similar to those in Fig. 2 (Supplementary Movies 1 and 2).

An important limitation of these and other short-period back-projections is that they are not directly sensitive to magnitude of fault slip (short-period seismic radiation is sensitive to slip-rate variations, and back-projection methods depend critically on wave field coherency, which can be high for spatially concentrated radiation from a small event and low for diffuse radiation from a large event)[22,23,28]. Thus, whereas the short-period results indicate multiple potential activated faults, the relative seismic moments of the fault segments are not resolved.

To overcome this deficiency, we used broadband surface waves to image spatial variations in seismic moment release, again allowing for the possibility of multiple fault segments. To account for complex surface wave propagation effects, we use global seismic recordings of short-arc Rayleigh waves (R_1) and Love waves (G_1) for a moderate size (M_w 7.2) event on 10 January 2012 with a source location (2.45° N, 93.21° E; 18:36:59 UTC) about 20 km northeast of the mainshock epicentre (Fig. 1), and a similar strike-slip focal mechanism. These signals are deconvolved from the corresponding M_w 8.7 and 8.2 great-event recordings to produce time series called source time functions[29] (STFs). The large earthquake rupture properties can be inferred by projecting the STFs into a space-time history of seismic radiation in essentially the same way as is done in short-period back-projections.

The spatial distributions of long-period seismic wave radiation imaged over a gridded region around the M_w 8.7 and 8.2 earthquake epicentres are shown in Fig. 3. Darker colours indicate stronger long-period source radiation, which tracks the aftershock distribution. There is some intrinsic smearing of the images due to the non-uniform and incomplete azimuthal coverage, and the spatial resolution is lower than for the short-period back-projections because we are dealing with one-sided moment rate functions and lower frequency signals; however, this method provides a better indication of seismic moment distribution. Plots of this imaging with R_1 and G_1 separately are shown in Supplementary Fig. 2.

For the M_w 8.7 event, the largest long-period source energy is concentrated near the epicentre, but there is significant source energy along both ESE–WNW aftershock trends, indicating either continuous rupture on corresponding faults or a sequence of discrete coseismically triggered 'early' aftershocks. The secondary features have peak amplitudes from 20–30% of the largest features, indicative of significant relative seismic moment. Snapshots of the reconstructed long-period radiation as a function of time are shown in Supplementary Fig. 3; these reveal rupture propagation in the WNW direction on both faults, and that the concentration of radiation almost 400 km west of the epicentre occurs at about 120 s. The relative STFs for the M_w 8.2 aftershock were similarly processed (Supplementary Fig. 4), and indicate source radiation concentrated near the hypocentre with rupture propagation towards the NNE. Comparison with Fig. 2 shows good agreement in map locations of source radiation for ~1 s period energy

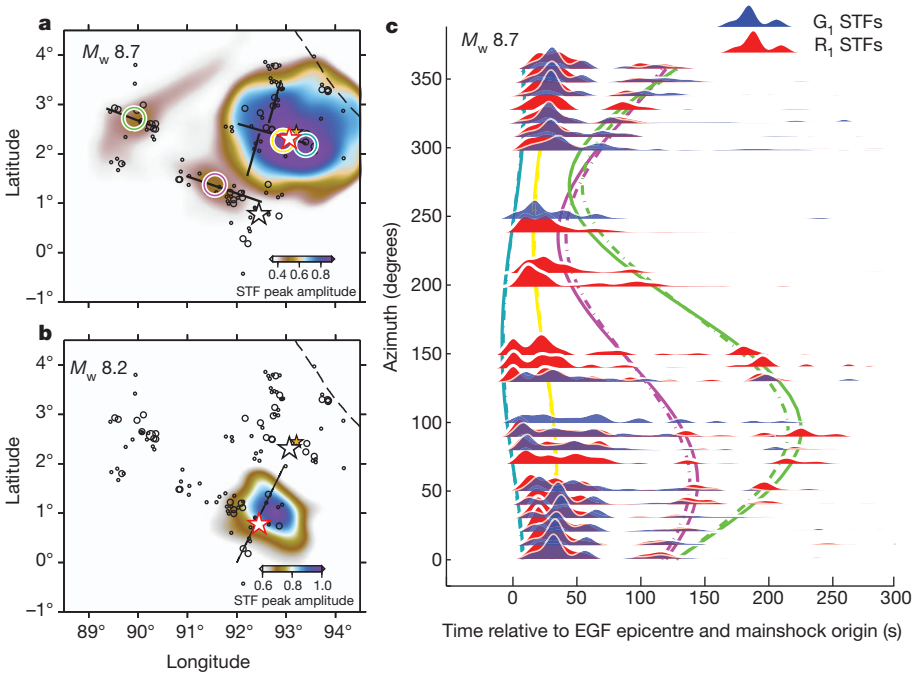

Figure 3 | Long-period seismic energy release pattern. **a**, **b**, Maps showing the spatial patterns of long-period surface wave energy sources for the 11 April 2012 (M_w 8.7) mainshock (**a**; epicentre indicated with a red outlined star) and the large (M_w 8.2) aftershock 2 h later (**b**; epicentre indicated with a red outlined star). The one-week aftershock distribution is shown by small circles with radii proportional to seismic magnitude. The colour images indicate the peak stacked energy at each position from combined R_1 source time functions (STFs) and G_1 STFs back-projected relative to the epicentral location of the 10 January 2012 (M_w 7.2) event (orange stars) which was used for empirical Green functions (EGFs). Solid lines indicate the orientations of likely subfaults that ruptured during each event. Snapshots that indicate the time history of energy release are shown in Supplementary Fig. 3. Coloured circles in the mainshock image indicate specific locations of energy release that produce arrivals considered in **c**, which shows the azimuthally binned and stacked R_1 (red) and G_1 (blue) STFs plotted in time relative to the EGF epicentre. These represent seismic moment as a function of time observed at different azimuths. The coloured curves correspond to the coloured circles in **a**, showing the predicted arrival times of energy from each location, with 'S-curve' patterns due to relative propagation times towards different azimuths. The solid curves are for R_1 waves using a velocity of 4.0 km s^{-1} and the dashed curves are for G_1 waves using a velocity of 4.5 km s^{-1}. The features aligned on such curves form the corresponding images in **a**, although images formed after 60 s of delay from the STF onsets have the first 60 s of the STFs masked out to avoid contamination. A corresponding profile of STFs for the M_w 8.2 aftershock is shown in Supplementary Fig. 4.

and ~20–200 s period energy, bolstering the interpretation that multiple faults with significant slip were activated during the main rupture. Neither imaging method provides depth resolution.

To resolve the spatial slip distribution, broadband teleseismic P and SH waves were inverted together with the surface wave STFs for finite-faulting models using multiple distinct fault segments inferred from the back-projections of short- and long-period seismic energy. Although single-fault inversions allow basic waveform features in the first 60 s to be fairly well modelled, the overall waveforms can be fitted better with additional fault complexity (and more parameters). Finite-fault inversions require specification of substantial a priori information about faulting geometry, rupture initiation time, rupture velocity, and discretization of the fault surface and subfault STFs. We use the consistency of the short-period and long-period imaging approaches in conjunction with the aftershock trends to specify four primary subfaults for the mainshock and one segment for the largest aftershock, with locations and timing of rupture initiation guided by the high-resolution short-period back-projections. Dip δ and rake λ orientations for each subfault with strike ϕ were constrained by extensive modelling and inversion suites.

Figure 4 shows the fault model geometry and the slip distributions obtained by least-squares inversion of P and SH waves using up to 200-s-long time windows of the seismograms (with some being truncated early to avoid contamination from PP and SS phases) along with the R_1 and G_1 STFs. Guided by the short-period back-projections, we specified the rupture velocity as 2.0 km s^{-1} on all segments. There is uncertainty in the kinematic parameters, but the collective information from aftershock locations and P wave and surface wave back-projections does provide first-order constraints.

Our results show that the great events of 11 April 2012 involve rupture of a very complex network of faults, for which we have no documented precedent in recorded seismic history. Good fits are found for the large P and SH wave and R_1 and G_1 data set (see Supplementary Fig. 5), although some secondary features are not fully accounted for. The failure process can be summarized as follows: first, a large moment release during a predominantly WNW-propagating, asymmetric bilateral strike-slip rupture (with 2.0 km s^{-1} velocity) with large peak slip (~37 m) and about 150 km total rupture length with seismic moment corresponding to M_w ~8.5. Second, this rupture triggered bilateral failure of a cross-cutting orthogonal fault that had a seismic moment corresponding to M_w ~7.9. Third, subsequent rupture occurred to the south on an *en échelon* ESE–WNW fault that expanded in the WNW direction with a seismic moment of M_w ~8.3. Fourth, the process culminated with a fourth activated fault segment about 300 km west of the epicentre that ruptured on either a WNW–ESE or NNE–SSW fault (or both) with M_w ~7.8 (Supplementary Fig. 6 shows the inversion results assuming the NNE–SSW orientation). The cumulative moment of these ruptures is 13.9×10^{21} N m, which gives M_w 8.7 (about 40% larger than point-source seismic moment estimates, and 15% larger than a two-subevent seismic moment estimate[30]). A modest non-double couple component is found when the individual subfault moment tensors are summed directly or allowing for temporal shifts (Supplementary Fig. 7).

Even allowing for the trade-offs and non-uniqueness of the very complex model description, it is well-established that this event activated a complex lattice of faults in the deformation zone between the India and Australia subplates, with the deep centroid depths, large estimated fault displacements and large extent of faulting of the sequence suggesting localization of deformation in the region extending westward from Sumatra to the Ninetyeast ridge. The shortening between the India and Australia subplates that is being accommodated across this deformation zone is mainly being distributed onto strike-slip faults rather than thrust faults, and the ultimate configuration of the plate boundary that will develop is difficult to anticipate. The failure process is somewhat influenced by the plate fabric, with NNE–SSW-trending structures embedded in the plate from its earlier

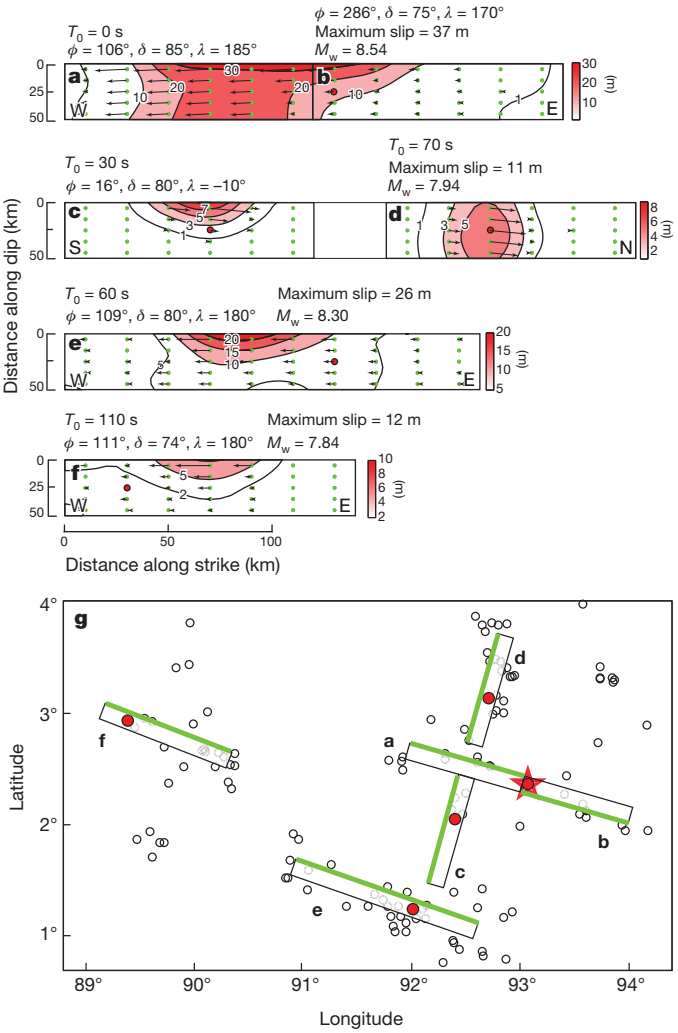

Figure 4 | Map of primary faulting during the M_w 8.7 event. **a**–**f**, Slip distributions on each subfault; **g**, map showing locations of subfaults. Map shows fault segments activated during the 11 April 2012 M_w 8.7 mainshock, specified for finite-fault slip model inversion of teleseismic broadband P and SH waves and R_1 and G_1 STFs. The faulting complexity is guided by the short-period and long-period source imaging in Figs 2 and 3 (and associated animations and time snapshots in the Supplementary Information) along with the one-week aftershock distribution. The red star indicates the epicentral location, and red dots indicate the placement of hypocentres (all at 30 km depth) on each fault segment. The rectangles indicate the subfault strikes and dips (shallow edge is on the green side, deeper edge on the black side. We use four subfaults (two of the subfaults are further subdivided) with onset times (T_0) constrained by the short-period back-projections. Slip distributions on each subfault (arrows indicate the relative size and direction of slip, with slip size colour contoured using the colour scale at right; green dots indicate the grid) are shown in **a**–**f**, with the subfault grids having 20 km spacing along-strike and 10 km spacing along-dip. The peak slip and M_w of each subfault is indicated, as is the position of the hypocentre on each subfault from which the rupture expands. The rupture velocity is 2.0 km s^{-1} for all subfaults. The M_w 8.2 event (epicentre given by black star) is not inverted because the broadband P and SH waves are obscured from surface waves from the first event, but it appears to involve bilateral rupture on a fifth fault, trending NNE–SSW. δ, dip; λ, rake; ϕ, strike.

formation probably providing zones of weakness that can fail in strike-slip events. However, the primary seismic moment is on WNW–ESE features, which cross-cut the trend of the Ninetyeast ridge. Large rupture through oceanic lithosphere cross-cutting fracture zones has been observed in the Antarctic plate[31]. High-resolution bathymetry swaths along the ridge have revealed many WNW–ESE fractures in the seafloor before the 2012 sequence[32], and these young features appear to

have dominated the faulting in this great earthquake sequence. Many more large fracturing events will be needed to evolve a localized plate boundary, so future extraordinary ruptures in the region may well occur, but this event currently stands as the largest-magnitude intra-plate strike-slip earthquake geophysicists have yet recorded.

METHODS SUMMARY

For a gridded distribution of possible rupture locations across the source region, short-period body waves and long-period surface waves from teleseismic stations were back-projected to image the space-time patterns of seismic wave radiation for the M_w 8.7 and 8.2 events, with minimal a priori assumptions about faulting geometry. Narrow-band filtered P waves from large aperture arrays in Europe and Japan were used to image locations of short-period radiation on the source grid using predicted travel-time variations across the arrays relative to an initial hypocentral alignment by shifting and fourth-root summing of the signals. Broadband R_1 Rayleigh waves and G_1 Love waves from global seismic stations were used to image the space-time locations of long-period seismic radiation. The complex dispersion effects of surface wave propagation were first removed using corresponding recordings from an M_w 7.2 earthquake on 10 January 2012 with very similar location and focal mechanism to the M_w 8.7 mainshock as empirical Green functions (EGFs). The EGF signals were deconvolved from the records of the large events, eliminating long-range propagation effects and extracting relative source time functions (STFs) for the large event. The STFs were then back-projected onto the source grid using average phase velocities for R_1 (4.0 km s^{-1}) and for G_1 (4.5 km s^{-1}). We then specified a set of four fault segments composed of multiple 10-km-wide by 20-km-long subfaults that activate at prescribed times (based on the short-period imaging), and invert broadband teleseismic P and SH waves and the surface wave STFs for finite fault slip distributions. The geometries of the segments are constrained by aftershock distribution and focal mechanisms, back-projections, and suites of inversions with varying parameters. The final model has time-varying slip on each fault segment consistent with the back-projection imaging, aftershocks, and broadband teleseismic signals.

Full Methods and any associated references are available in the online version of the paper.

Received 6 May; accepted 7 August 2012.
Published online 26 September 2012.

1. Minster, J. B. & Jordan, T. H. Present day plate motions. *J. Geophys. Res.* **83,** 5331–5354 (1978).
2. Wiens, D. *et al.* A diffuse plate boundary model for Indian Ocean tectonics. *Geophys. Res. Lett.* **12,** 429–432 (1985).
3. Gordon, R. G., DeMets, C. & Argus, D. F. Kinematic constraints on distributed lithospheric deformation in the equatorial Indian Ocean from present motions between the Australian and Indian plates. *Tectonics* **9,** 409–422 (1990).
4. Gordon, R. G. DeMets, C. & Royer, J.-Y. Evidence for long-term diffuse deformation of the lithosphere of the equatorial Indian Ocean. *Nature* **395,** 370–374 (1998).
5. Royer, J.-Y. & Gordon, R. G. The motion and boundary between the Capricorn and Australian plates. *Science* **277,** 1268–1274 (1997).
6. Stein, S. & Okal, E. A. Seismicity and tectonics of the Ninetyeast Ridge area, evidence for internal deformation of the Indian Plate. *J. Geophys. Res.* **83,** 2233–2245 (1978).
7. Delescluse, M. & Chamot-Rooke, N. Instantaneous deformation and kinematics of the India-Australia plate. *Geophys. J. Int.* **168,** 818–842 (2007).
8. DeMets, C. & Royer, J.-Y. A new high-resolution model for India-Capricorn motion since 20 Ma: implications for the chronology and magnitude of distributed crustal deformation in the Central Indian Basin. *Curr. Sci.* **85,** 339–345 (2003).
9. Robinson, D. P., Henry, C., Das, S. & Woodhouse, H. H. Simultaneous rupture along two conjugate planes of the Wharton Basin earthquake. *Science* **292,** 1145–1148 (2001).
10. Abercrombie, R. E., Antolik, M. & Ekström, G. The June 2000 M_w 7.9 earthquakes south of Sumatra: deformation in the India-Australia Plate. *J. Geophys. Res.* **108** (B1), 2018, http://dx.doi.org/10.1029/2001JB000674 (2003).
11. McGuire, J. J. & Beroza, G. C. A rogue earthquake off Sumatra. *Science* **336,** 1118–1119 (2012).
12. Kanamori, H. The energy release in great earthquakes. *J. Geophys. Res.* **82,** 2981–2987 (1977).
13. Ben-Menahem, A., Aboodi, E. & Schild, R. The source of the great Assam earthquake — an interplate wedge motion. *Phys. Earth Planet. Inter.* **9,** 265–289 (1974).
14. Chen, W.-P. & Molnar, P. Seismic moments of major earthquakes and the average rate of slip in Central Eurasia. *J. Geophys. Res.* **82,** 2945–2969 (1977).
15. Molnar, P. A review of the seismicity and the rates of active underthrusting and deformation at the Himalayas. *J. Himal. Geol.* **1,** 131–154 (1990).
16. Pollitz, F. F., Stein, R. S., Sevilgen, V. & Bürgmann, R. The 11 April 2012 east Indian Ocean earthquake triggered large aftershocks worldwide. *Nature* http://dx.doi.org/nature11504 (this issue).
17. Ammon, C. J. *et al.* Rupture process of the 2004 Sumatra-Andaman earthquake. *Science* **308,** 1133–1139 (2005).
18. Delescluse, M. *et al.* April 2012 intra-oceanic seismicity off Sumatra boosted by the Banda–Aceh megathrust. *Nature* http://dx.doi.org/nature11520 (this issue).
19. Shapiro, N. M., Ritzwoller, M. H. & Engdahl, E. R. Structural context of the great Sumatra-Andaman Islands earthquake. *Geophys. Res. Lett.* **35,** L05301, http://dx.doi.org/10.1029/2008GL033381 (2008).
20. Ishii, M., Shearer, P. M., Houston, H. & Vidale, J. E. Extent, duration and speed of the 2004 Sumatra-Andaman earthquake imaged by the Hi-net array. *Nature* **435,** 933–936 (2005).
21. Krüger, F. & Ohrnberger, M. Tracking the rupture of the M_w 9.3 Sumatra earthquake over 1,150 km at teleseismic distance. *Nature* **435,** 937–939 (2005).
22. Koper, K. D., Hutko, A. R., Lay, T. & Sufri, O. Imaging short-period seismic radiation from the 27 February 2010 Chile (M_w 8.8) earthquake by back-projection of P, PP, and PKIKP waves. *J. Geophys. Res.* **117,** B02308, http://dx.doi.org/10.1029/2011JB008576 (2012).
23. Koper, K. D., Hutko, A. R. & Lay, T. Along-dip variation of teleseismic short-period radiation from the 11 March 2011 Tohoku Earthquake (M_w 9.0). *Geophys. Res. Lett.* **38,** L21309, http://dx.doi.org/10.1029/2011GL049689 (2011).
24. Incorporated Research Institutions for Seismology. Back projections for M_w 8. 7 off W coast of Northern Sumatra, http://www.iris.edu/spud/backprojection/118733 (2012).
25. Meng, L., Ampuero, J.-P. & Luo, Y. Back-projection results, 4/11/2012 (Mw8.6) offshore Sumatra, Indonesia. http://www.tectonics.caltech.edu/slip_history/2012_Sumatra/back_projection/.
26. Kiser, E. Preliminary rupture modeling of the April 11, 2012 Sumatran earthquakes. http://www.seismology.harvard.edu/research_sumatra2012.html.
27. Wang, D., Mori, J. & Ohmi, S. Rupture process of the April 11, 2012 Sumatra (Mw 8.6) earthquake imaged with back-projection of Hi-net data. http://www.eqh.dpri.kyoto-u.ac.jp/src/etc/sumatra.htm.
28. Lay, T. *et al.* Depth-varying rupture properties of subduction zone megathrust faults. *J. Geophys. Res.* **117,** B04311, http://dx.doi.org/10.1029/2011JB009133 (2012).
29. Lay, T. *et al.* The 2006–2007 Kuril Islands great earthquake sequence. *J. Geophys. Res.* **114,** B11308, http://dx.doi.org/10.1029/2008JB006280 (2009).
30. Duputel, Z. *et al.* The 2012 Sumatra great earthquake sequence. *Earth Planet. Sci. Lett.* **351-352,** http://dx.doi.org/10.1016/j.epsl.2012.07.017 (2012).
31. Hjörleifsdóttir, V., Kanamori, H. & Tromp, J. Modeling 3-D wave propagation and finite slip for the 1998 Balleny Islands earthquake. *J. Geophys. Res.* **114,** B03301, http://dx.doi.org/10.1029/2008JB005975 (2009).
32. Meng, L. *et al.* Earthquake in a maze: compressional rupture branching during the 2012 M_w 8.6 Sumatra earthquake. *Science* **337,** 724–726 (2012).

Supplementary Information is available in the online version of the paper.

Acknowledgements We thank H. Kanamori, Z. Duputel and G. Hayes for discussions and exchanges of information about this event. A. Hutko provided early short-period back-projection results. We thank R. Abercrombie for comments on this paper. This work made use of GMT and SAC software and Federation of Digital Seismic Networks (FDSN) seismic data. The Incorporated Research Institutions for Seismology (IRIS) Data Management System (DMS), the European ORFEUS Data Center and the NIED F-net Data Centre were used to access the data. This work was supported by NSF grant EAR0635570 (T.L.) and EAR0951558 (K.D.K.).

Author Contributions H.Y. contributed to the surface wave back-projections and finite fault modelling; K.D.K. performed the short-period back-projections; and T.L. performed finite-fault inversions and guided the synthesis.

Author Information Reprints and permissions information is available at www.nature.com/reprints. The authors declare no competing financial interests. Readers are welcome to comment on the online version of the paper. Correspondence and requests for materials should be addressed to T.L. (tlay@ucsc.edu).

METHODS

Short-period back-projection imaging. Back-projections of short-period teleseismic P waves were carried out for the M_w 8.7 and M_w 8.2 earthquakes of 11 April 2012 using large aperture arrays of seismometers drawn from various European broadband seismic networks and the F-net array of broadband seismometers in Japan. In each of the four cases, conventional time-domain back-projection[33] was used with a spatial grid bounded in longitude by 88°–96° E and in latitude by 1° S–6° N, using 0.1° increments. The depth was held fixed at the nominal USGS hypocentral values of 23 km and 16 km, for the mainshock and aftershock, respectively. Stacked seismogram beam power was calculated using fourth-root stacking over a tapered, 10-s-long window that was shifted in increments of 1 s. Time shifts for back-projecting the seismic energy to the source region were calculated for the AK135 reference model[34], and initial static station corrections were derived using multi-channel cross-correlation[35] (MCCC) of the initial 10 s of P-wave energy.

For the European back-projection of the M_w 8.7 event, 196 vertical broadband channels in the distance range of 43°–100° were downloaded from the ORFEUS Data Center (www.orfeus-eu.org). The data were examined for quality and ultimately 85 seismograms, each with a mean cross-correlation value >0.7 from an MCCC analysis of unfiltered traces, were selected for back-projection. The data were filtered into passbands of 0.5–2.0 Hz and 0.1–0.5 Hz for separate back-projections. Some stations with high-quality data were not used because they were redundant with other nearby high-quality stations. We checked that the array response[31] of the final configuration was more compact and symmetric than that corresponding to using all viable European data (a total of 157 traces). The final data set includes traces in the distance range 55° to 95°. The same set of 85 stations was used in back-projecting data from the M_w 8.2 event, although static station corrections were recalculated with MCCC for the initial 10 s of energy in a passband of 0.2–2.0 Hz, achieving a minimum mean correlation coefficient of 0.6. The similarity of the M_w 8.2 P waves was degraded by coda from the mainshock and MCCC analysis on unfiltered traces was not viable. The root-mean-square difference in the two sets of statics is 0.13 s, and back-projections of the M_w 8.2 event data using the statics for the M_w 8.7 event gives similar results to what is shown in this Letter, although there is a slight southward translation of the beam power.

For the back-projection of F-net data for the M_w 8.7 event, 72 vertical, broadband channels in the distance range of 36°–62° were downloaded from the NIED data centre (www.fnet.bosai.go.jp). The data were examined for quality and ultimately 67 seismograms, each with a mean cross-correlation value >0.88 from an MCCC analysis of unfiltered traces, were selected for back-projection. The aligned data were filtered in the passband 0.5–2.0 Hz for stacking. Because of the quasi-regular spacing of F-net stations, no seismograms were deleted in an effort to improve the array response and equalize data importance. The higher similarity of the Japan P waves compared to European P waves is offset by the smaller aperture of F-net and we consider the European results to be more robust. The same 67 stations were used to back-project the M_w 8.2 event data, but again with statics newly derived from MCCC analysis of the initial 10 s of P-wave energy. As with the European data, similarity was lower than for the mainshock, with a minimum mean correlation coefficient of 0.52, and the root-mean-square difference in the two sets of statics was 0.27 s. Nevertheless, Japan back-projections for the M_w 8.2 data using statics for the mainshock again give results similar to what are shown in this Letter.

Surface wave STF imaging. Surface waves that travel along the short great-circle arc (R_1 Rayleigh waves and G_1 Love waves) from the source region to broadband seismic stations around the world are used to image the space-time locations of long-period seismic radiation from the M_w 8.7 and M_w 8.2 events. Group velocity windows that varied with epicentral distance were used to isolate the fundamental mode energy from overtones and long-arc arrivals. To remove the complex dispersion, attenuation, and focusing effects of surface wave propagation, R_1 and G_1 recordings from an M_w 7.2 earthquake that occurred on 10 January 2012 with very similar location and focal mechanism to the M_w 8.7 mainshock are used as empirical Green functions (EGFs)[36]. We inverted P waves for the EGF event to ensure that the catalogue focal mechanism was correct and to establish that the source process was not anomalous. The individual horizontal component instrument responses were deconvolved before rotation for the G_1 waves, ensuring good isolation of the transverse motions. The rotated G_1 signals were bandpass filtered in the passband 0.005–1.0 Hz. We used 525 Rayleigh waves and 485 Love waves for the final analysis. Only stations at distances less than 150° were used to avoid contamination from the R_2 and G_2 arrivals. Visual comparisons of low-pass filtered traces of all of the EGF and large event signals were made to ensure adequate signal coherence and long-period signal stability, retaining stable signals away from radiation nodes. The selected EGF signals were deconvolved from the corresponding records of the large events using an iterative time-domain deconvolution procedure with a positivity constraint[29]. This eliminates long-range dispersive propagation effects and yields relative source time functions (STFs), which indicate the difference in overall source radiation time history for the large events relative to the EGF. The relative STFs were then convolved with an estimate of the STF for the EGF event obtained by finite-fault inversion of P waves, giving absolute STFs for the main shock. A 20 s corner low-pass filter was applied to remove short-period signal components from all STFs.

The surface wave STFs were averaged in 10° azimuthal windows, then back-projected over a source grid similar to that for the short-period P wave procedure, but using average phase velocities of 4.0 km s^{-1} for R_1 and 4.5 km s^{-1} for G_1. These phase velocities are appropriate for about 80 s period waves, which are in the centre of the passband of the deconvolved signals. There can be some distortion of the STFs due to variation in propagation distances for a finite source, and this effect increases with source location difference from the EGF location, but the basic character of the STFs is preserved by the positivity constraint in the deconvolution. In the stacking, we applied azimuthal weighting of the STFs for R_1 and G_1 proportional to the $\sin(2\theta)$ and $\sin(2\theta + 45°)$ azimuthal radiation patterns for strike-slip events, downweighting STFs for near-nodal directions where small errors in the EGF can produce unstable STF estimates. STF features that have systematic move-out of arrivals at azimuthally distributed stations sum constructively for corresponding source space-time locations. This provides images of where long-period radiation emanated from the source region independent of assumption of any particular fault configuration, although we assume the focal mechanisms are consistent with the EGF. The relative stack amplitudes are indicative of relative seismic moment of secondary sources in the rupture process, but some uncertainty is produced by the possibility of small errors in the EGF geometry between subevents, differential path length attenuation effects, and interference with arrivals from other subevents. Experiments with simulations indicate good (~10%) recovery of localized subevent moment under favourable imaging conditions.

Finite fault slip model inversion. Given the complex space-time distributions of source radiation indicated by the short-period P-wave and long-period R_1 and G_1 STF back-projections, along with the correlated aftershock distribution, we specify a set of fault segments composed of multiple 10-km-wide by 20-km-long subfaults extending from the ocean floor (below a 5-km-thick ocean layer) to ~55-km depth that activate at prescribed times (based on the short-period imaging), and invert broadband teleseismic P and SH waves for finite fault slip distributions. The geometries of the segments are constrained by aftershock distribution and focal mechanisms, back-projections, and suites of inversions with varying parameters.

The rupture initiates at 30 km depth on each fault segment. Resolution of hypocentral depths is poor, but the choice was made based on the 30–50 km centroid depths found in very long-period (>200 s) point-source inversions for this event, suggestive of rupture extending throughout the oceanic lithosphere. We specify rupture velocity as 2 km s^{-1} for each segment guided by the back-projections, and allow a flexible parameterization of the source functions on each subfault. For fault segments (a,b,c,d,f) each subfault STF is parameterized with seven symmetric 3-s rise time triangles offset by 3-s each, allowing total subfault durations of 24 s, whereas fault segment e has subfaults with five similar triangles with total allowed subfault durations of 18 s. The complexity of slip does not provide tight constraints on the subfault durations.

Based on many modelling efforts, we specify the rake on each subfault, allowing us to invert the body waves and surface wave STFs simultaneously. Fault dip was specified after performing inversions for a range of values. We found that allowing the dip to vary from the eastern half to the western half of the first fault enabled significant improvement in fit to P waveforms at azimuths to the WSW. For most fault segments the body wave inversion concentrates seismic moment and, hence, slip in the upper three rows of each fault model (depths of 5–35 km below ocean surface), spanning the thin oceanic crust and uppermost mantle layer, but deeper slip is found on several of the segments, notably segment a. Relative to the P waves, the SH signals are weighted by a factor of 0.2 to balance their amplitudes, while relative to the body waves the surface wave STFs are weighted by a factor of 5 to ensure good constraint on the total moment. The residual waveform mismatch power is 29% for the body waves and 19% for the STFs. The final result is a model of time-varying slip on each fault segment consistent with the back-projection imaging, aftershocks, and broadband teleseismic signals. The many parameters in such a complex model make the finite-source kinematic slip inversion even more non-unique than for single fault models, so it is best viewed as a plausible realization of overall rupture process for the event.

33. Xu, Y., Koper, K. D., Sufri, O., Zhu, L. & Hutko, A. R. Rupture imaging of the M_w 7.9 12 May 2008 Wenchuan earthquake from back projection of teleseismic P waves. *Geochem. Geophys. Geosyst.* **10,** Q04006 (2009).
34. Kennett, B. L. N., Engdahl, E. R. & Buland, R. Constraints on seismic velocities in the Earth from travel times. *Geophys. J. Int.* **122,** 108–124 (1995).
35. VanDecar, J. C. & Crosson, R. Determination of teleseismic relative phase arrival times using multi-channel cross-correlation and least squares. *Bull. Seismol. Soc. Am.* **80,** 150–159 (1990).
36. Velasco, A. A., Ammon, C. J. & Lay, T. Empirical Green function deconvolution of broadband surface waves: Rupture directivity of the 1992 Landers, California (M_w 7.3) earthquake. *Bull. Seismol. Soc. Am.* **84,** 735–750 (1994).